Surface properties and thermal stability of SiO2-crystalline TiO2 nano-composites

Magali Bonne, Stéphane Pronier, Yann Batonneau, Fabien Can, Xavier Courtois, Sébastien Royer, Patrice Marécot, Daniel Duprez

Surface properties and thermal stability of SiO_2-crystalline TiO_2 nano-composites

M. Bonne, S. Pronier, Y. Batonneau, F. Can, X. Courtois, S. Royer,[†] P. Marécot, D. Duprez

LACCO, UMR 6503 CNRS, 40 Avenue du Recteur Pineau, 86022 Poitiers Cedex France.

[†], Author to whom correspondence should be addressed: Tel.: +33-(0)5-49-45-34-79; Fax: +33-(0)5-49-45-37-41; E-mail: sebastien.royer@univ-poitiers.fr

Keywords: titania nanocomposite, mesoporous silica, thermal stability, surface properties, oxygen mobility.

Abstract

TiO_2/SiO_2 nanocomposites are synthesized and fully characterized after thermal stabilization at temperatures between 400°C and 800°C. The control of the impregnation media is crucial to obtain nanocomposites of satisfactory quality, i.e. presenting no segregation of titania particles outside the silica pore structure. Characterization shows that pore size and pore volume decrease linearly with an increase in titania loading, and remain close to the theoretical values calculated assuming the formation of a non-porous coating. Surface area remains unchanged whatever the titania loading (always comprised between 450 and 480 $m^2\ g^{-1}$), and micropore volume evolution suggests the formation of nanometric particles within the silica pores. While X-ray diffraction is inefficient to identify the titania phase, Raman spectroscopy showed the formation of anatase particles, with crystal sizes in the nanometric range (<4.5 nm, when stabilized at 400°C). Satisfying thermal stability is obtained on the low titania loading nanocomposites (20 wt% TiO_2), with only minor anatase crystal growth up to 800°C. Further characterization by FT-IR of the surface chemical properties of the nanocomposites showed properties similar to that of conventional titania, while improved oxygen mobilities (as evaluated by the $^{18}O/^{16}O$ exchange reaction) are reported on the low titania loading, thermally stable,

composites.

Introduction

Semiconducting transition metal (TM) oxides are used for a wide variety of photocatalytic reactions. Among the semiconducting TM oxides, titanium dioxide is by far the most studied one. Titania exists as different polymorphs (*e.g.* rutile, anatase, brookite) presenting different chemical and physical properties.[1-3] Indeed, crystal domain of nanometric size can be obtained from the anatase structure of titania while phase transition from anatase to rutile generally results in a large increase in crystal domain size,[4] engendering a decrease in accessible surface area with the logical consequences on the catalytic activities. In addition, the low specific surface area developed by the rutile is an important drawback for the dispersion of an active phase (like noble metal or oxide) on its surface. All these specificities explain why the anatase form of titania is generally chosen for academic studies in many fields of catalysis such as gas phase depollution,[5,6] energy conversion,[7,8] hydrodesulfurization[9,10] and fine chemistry[11,12].

The synthesis of titania having high surface area, open porosity, and acceptable thermal stability is a real challenge for the catalysis community. Different routes of synthesis are reported in the literature, such as precipitation from inorganic salts.[13,14] Unfortunately, solids obtained from these procedures present physical properties of limited interest. Indeed, surface areas rarely exceed 150 $m^2.g^{-1}$ when samples are calcined for a sufficient time at temperatures compatible with the catalytic applications. Other synthesis routes, such as sol-gel procedures,[15,16] allow the production of solids having increased surface areas. Unfortunately, anatase to rutile transition always occurred at 450-550°C,[17] and no improvement in thermal stability was reported. Due to the recent developments made in the field of solid mesotructuration, the synthesis of mesostructured TiO_2 was reported using different templating approaches. Neutral / non ionic or cationic templates were then used as templating agent to obtain TiO_2 with "*regular*" porosity and high surface area. Unfortunately, most of the studies reported a poor structuration of the titania samples, even if surface areas can reach several hundred square meters per grams. Generally, surface areas obtained using block copolymers as templates remained lower than when using a primary amine,[22–31] and thermal stability remained unchanged. Encouraging results concerning thermal stability were only obtained using cationic surfactants such as

cetyltrimethylammonium bromide[32–34] or by proposing post-treatment or surface post-grafting procedures.[21,35,36]

For an application in heterogeneous catalysis, such as hydrodesulfurization or gas phase depollution, support thermal stability up to 600–700°C is needed. At these temperatures, mesostructured silica supports are stable and can be used as host support for the incorporation of heteroatoms, or dispersion of nanocrystals on their surfaces. This approach combines the advantages of the silica support (open porosity and thermal stability) with the properties of titania nanoclusters (improved accessible surface if homogeneous dispersion is obtained in the support). Thus, procedures for the incorporation or deposition of titania in mesostructured silica were developed concurrently to the synthesis of bulk mesostructured titania. For direct incorporation of Ti atoms in the silica walls during synthesis, careful control of the synthesis conditions (i.e. acid concentration, conditions of hydrothermal treatment etc.) is needed to avoid segregation of titania in the form of large external particles.[37–41] Even under careful control of the synthesis media, formation of nanoparticles on the surface of the mesopores[37,39] or embedded in the walls[38] can lead to some channel blocking. Such nanocomposites however exhibited considerably improved thermal stability with respect to that of bulk TiO_2.[37,38] Another proposed way to obtain Ti–Si composites is the post-grafting of titania on a preformed silica support.[42–45] Incorporation of titania at low loading generally leads to a satisfying dispersion of Ti atoms in the pore structure, avoiding the detection of anatase reflection by XRD.[44] Unfortunately, thermal stabilization can lead to an important decrease in specific surface area.[46] Such TiO_2-SiO_2 nanocomposites found applications and interests in many fields, such as photocatalytic and catalytic applications.[47–53] It has been shown that titania clusters are still active even inside the silica framework, while the importance of the titania particle size is clearly demonstrated by the decrease in catalytic activity with the aggregation of the clusters.

In this work titania nanocrystals dispersed in a large pore SBA-15 support are synthesized. Composites of different TiO_2/SiO_2 mass ratios (up to 1.22, *i.e.* 55 wt% TiO_2 in the composite) are prepared using impregnation of titanium alkoxide in a short chain alcohol, and are characterized by

TEM, N_2-sorption experiments, XRD, FT-IR and Raman spectroscopy in order to accede to a satisfying description of the composite morphologies. Finally, thermal stabilities of selected samples are evaluated up to 800°C, and oxygen reactivity measured for the most promising solids.

Experimental section

The regular pore structure of the mesostructured materials makes these solids ideal supports for impregnation. Due to the easiness of the SBA15-type silica synthesis, this solid is chosen as a host support. In order to obtain homogeneous composites, *i.e.* presenting a high dispersion of titania nanoparticles on the silica surface, an impregnation procedure using an alkoxide precursor is chosen. The nomenclature used for the composites is defined as follow:

yTi-SBA-c**XXX**

With: **y**, TiO_2 content (in wt.%)

XXX, calcination temperature (°C)

For the synthesis, all chemicals are used as received. Poly(ethylene oxide)-*b*-poly(propylene oxide)-*b*-poly(ethylene oxide) $EO_{20}PO_{70}EO_{20}$ (Pluronic P123), Titanium (IV) isopropoxide ($Ti(O^iPr)_4$, 97%) and hydrochloric acid (HCl, 32 wt.%) were purchased from Aldrich. Tetraethyl orthosilicate (TEOS, ≥99%) was purchased from Fluka. Anhydrous ethanol (> 99.9%) was purchased from Merck.

Synthesis of the host support (SBA, Table 1)

The SBA-15 support is prepared according to the procedure proposed by Roggenbuck et al.[46] A mass of 12.0 g of triblock copolymer P123 is dissolved in 360 g of distilled water and 43 g of HCl 32 wt.%. The solution is heated at 35 °C. After 1 hour to ensure the complete dissolution of the copolymer, 24 g of TEOS is slowly added under vigorous stirring, given a synthesis composition 1 TEOS : 0.018 P123 : 3.3 HCl : 187 H_2O (molar ratio). The transparent solution is stirred at 35 °C for 24 h, and the milky solution obtained is transferred in a Teflon-line autoclave for treatment at 140 °C for 24 h. The autoclave is cooled down to room temperature, and the white solid filtered, washed with distilled water,

and dried at 80 °C overnight. Before use and characterization, the solid is calcined under air at 550 °C for 3 h (temperature increase ramp = 1 °C.min^{-1}).

Composite synthesis

In all case, the freshly calcined SBA-15 is used as a silica host support and titanium isopropoxide ($Ti(O^iPr)_4$) as titanium source. Sample preparation consists in the slow impregnation of a dilute solution of $Ti(O^iPr)_4$ in dry ethanol. A solution of $Ti(O^iPr)_4$ / ethanol (volume ratio $V_{Ti(OiPr)4}/V_{EtOH}$ = 0.2 at room temperature) is first prepared (solution S). A known volume of S (depending on the desired titania loading) is then slowly added to the silica support. The solvent is evaporated under stirring at room temperature, and the solid aged one day under ambient conditions. Thereafter, the aged solid is transferred into an oven at 80 °C for one night. If necessary, impregnation procedure is repeated a second time to obtain high TiO_2 content (sample 55Ti-SBA, Table 1). After drying, nanocomposites are calcined 3 h at 400 °C (temperature increase rate = 1 °C.min^{-1}).

Characterization

Specific surface area, pore size distribution and pore volume are obtained from N_2 adsorption-desorption experiments. A known mass of about 0.150 g of sample is first heated under vacuum 6 h at 250 °C. Isotherms are obtained at -196 °C on a TRISTAR instrument from Micromeritics. The specific surface area, S_{BET}, was determined from the linear part of the BET plot. The mesopore size distribution was determined by the non local density functional theory (NLDFT) method and calculated using the Autosorb-1 1.52 software. The kernel selected was N_2 on silica assuming cylindrical pore geometry and the equilibrium based on the desorption branch. Pore volume is determined on the isotherms at P/P_0 = 0.97.

Powder XRD patterns are collected on a Bruker AXS D5005 X-ray diffractometer, using a CuKα radiation (λ = 1.54184 Å) as X-ray source. For small angle analysis, signal is recorded for 2θ comprised between 0.75 ° and 5 ° with a step of 0.01 ° (step time of 10 s). For wide angle analysis, signal is recorded for 2θ comprised between 10 ° and 80 ° with a step of 0.05 ° (step time of 2 s). Phase identification was made by comparison with JCPDS database. If diffraction peaks assigned to the

anatase form are detected in the 10-80 ° region, crystal domain size is estimated using the Scherrer equation after Warren's correction for instrumental broadening: $D = \frac{K.\lambda}{\beta.\cos\theta}$. K is a constant assumed equal to 0.86 and λ is the wavelength of the X-ray source. β is the effective linewidth of the X-ray reflection, calculated by the formula $\beta^2 = B^2 - b^2$ where B is the full width at half maximum (FWHM) of the reflection and b is the instrumental broadening determined by the FWHM of X-ray reflection of quartz having particles larger than 150 nm.

The pore structure, as well as TiO_2 particle distribution inside the silica grain, is evaluated by Transmission Electronic Microscopy (TEM) coupled with Energy Dispersive X-ray Spectroscopy (EDXS). Micrographs are obtained on a JEOL 2100 instrument (operated at 200 kV with a LaB_6 source and equipped with a Gatan Ultra scan camera). EDX spectroscopy is carried out with a Hypernine (Premium) detector (active area: 30 mm^2) using the software SM-JED 2300T for data acquisition and treatment. Analysis zone is defined on the middle of micrometric silica particles, and is generally ranging from 80 nm to 100 nm. Analysis is repeated on several silica grains to accede to a mean value of TiO_2/SiO_2 ratio. This allows to verify if impregnation results in a satisfying dispersion of titania into the different silica grains or segregates at the outer layers of silica.

Raman spectra (Stokes spectra) are obtained at room temperature, using an HR UV 800 confocal scanning spectrometer (Horiba Jobin Yvon) equipped with a Peltier-cooled charge coupled device (1152 × 298 pixels) used for detection. The Raman scattering is excited using a 514.52 nm excitation wavelength supplied by an external, air-cooled, Ar^+ laser (Melles Griot) through an Olympus high-stability BXFM microscope coupled confocally. Laser power delivered at the sample (*ca.* 20 mW without filtering) can be monitored via a filters' wheel with optical densities of 0.3, 0.6, and 1. The backscattered radiation is collected using the same microscope with a 50× Olympus objective (numerical aperture 0.55). An 1800 grooves mm^{-1} holographic grating is used and the confocal hole aperture is 300 µm, resulting in an instrumental bandwith of 6.3 cm^{-1} and a spectral resolution of 0.5 cm^{-1} in the 50-1000 cm^{-1} Raman shift range. The spectrometer was calibrated using the Γ_{25} phonon of

diamond Si (Fd-3m) resulting in an accuracy of less than 0.5 cm^{-1}. LabSPEC v.5 software is used to perform both acquisition and data processing.

IR spectra are recorded on a Nicolet Nexus spectrometer equipped with a DTGS detector (Deuterium TriGlyceride Sulfur) and a KBr beamsplitter using a resolution of 4 cm^{-1} and 64 scans. Samples were pressed as self-supported wafers and activated in a dedicated cell under oxygen flow (100 $mL.min^{-1}$) up to 400 °C (temperature increase rate = 5 $°C.min^{-1}$) for 1 h, before being evacuated under dynamic vacuum for 15 min. Infrared spectra presented are normalized to a disc of 10 $mg.cm^{-2}$. The silanol (SiOH) stretching band surface is deduced from spectra decomposition, using the peak solve fitting from OMNIC. Peak type is fixed to a Gaussian/Lorentzian function centered at 3745 ± 5 cm^{-1}, with a maximum full width at half height (FWHM) of 15 cm^{-1}. Residual TiOH area is estimated by substraction of the SiOH area to the total free OH area, assuming contributions of SiOH and TiOH as purely additive. The determination of the OH surface density is calculated using the Beer-Lambert law:

$$n(\mathrm{OH}) = \frac{\mathrm{A} \times \mathrm{S} \times N_{\mathrm{A}}}{\varepsilon \times \mathrm{S}_{\mathrm{BET}} \times \mathrm{m}}$$

Where ε is the molar absorption coefficient for the SiOH species, equal to 1 $cm.mol^{-1}$ at 3750 cm^{-1}, *n(OH)* is the OH surface density ($OH.nm^{-2}$), A is the IR absorbance (cm^{-1}), S is the surface of the self-supported wafer (cm^2), N_A is the Avogadro's number, S_{BET} is the specific surface area ($m^2.g^{-1}$), and m the weight of the wafer (g).

The oxygen isotopic exchange (OIE) reaction is used to evaluate oxygen mobility in the composites, and in a reference bulk TiO_2 sample (P25, Degussa). Full description of the exchange test and data treatment can be found elsewhere,[47,48] and is only summarized here. The exchange mechanism can be described by the following equation, even if different mechanisms are depicted: $^{18}O_g + {}^{16}O_s \rightarrow {}^{16}O_g + {}^{18}O_s$, where s and g refer to oxygen from the solid and from the gas phase respectively. For the exchange experiment, an equivalent of 20 mg of TiO_2 is inserted in a microreactor, and heat treated up to 400 °C under O_2 (ramp = 5 $°C.min^{-1}$, Q_{O2} = 50 $mL.min^{-1}$). The sample is then evacuated, and 65 mbar of pure $^{18}O_2$ introduced in the cell. The experiment is performed from 400°C to 800°C (ramp =5 $°C.min^{-1}$), and

partial pressure evolution of $^{18}O_2$ (mass 36), $^{16}O_2$ (mass 32), and $^{16}O^{18}O$ (mass 34) are recorded on a mass spectrometer allowing quantification of the ^{18}O fraction in the gas phase (α), the number of oxygen atom exchanged (N_{ex}), and the fraction of the solid exchanged at the end of the experiment (O_{ex}).

Results and discussion

Properties of the silica host support

Since the synthesis of SBA-15 is widely reported in the literature, and its physical properties are well known, the properties obtained for the host support are only summarized. A type IV isotherm,[57] with parallel adsorption and desorption branches and a long adsorption plateau at high P/P_0, (Fig. S1A†), and a narrow pore size distribution (Fig. S1B†) are obtained. The N_2 pore volume is higher than 1 cm^3 g^{-1} and t-plot shows the presence of microporosity originating from the hydrophilic nature of poly(ethylene oxide) (PEO) blocks of the template.[58,59] Due to the high hydrothermal treatment temperature, micropore fraction remains limited (Table 1). X-Ray diffraction pattern shows three diffraction peaks in the 1–3° region (Fig. S2A†), indexed to the (100), (110) and (200) reflections of the P6mm hexagonal pore structure. The corresponding lattice spacing estimated on the (100) diffraction peak is 9.1 nm (Table 1). A well organized material (having regular pore channels) is observed by TEM, whatever the zone of the sample analyzed (Fig. 1A, B).

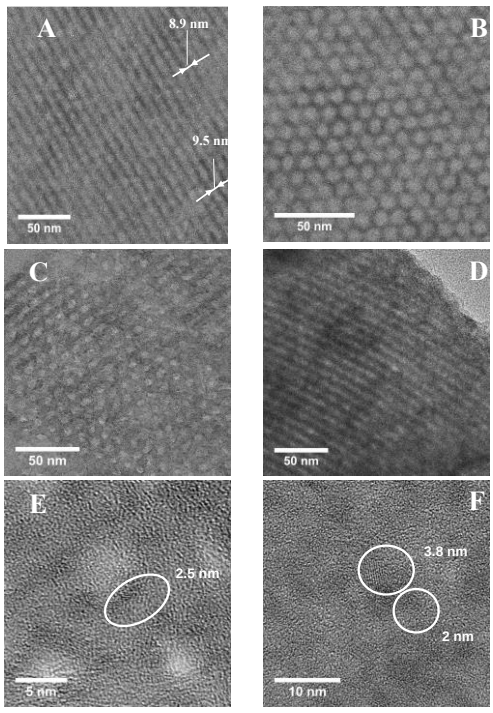

Fig. 1. TEM images obtained over the different nanocomposites. (A) and (B) SBA-15; (C) and (E), 20Ti-SBA-c400 composite; (D) and (F), 55Ti-SBA-c400 composite.

Nanocomposites physical properties

The physical properties obtained for the different composites are summarized in Table 1, and N_2 adsorption-desorption isotherms presented in Fig. S1A†. A type IV isotherm according to the IUPAC classification is always obtained whatever the TiO_2 loading. A slight evolution in the hysteresis form from H1 type (with parallel adsorption and desorption branches, characteristic of cylindrical pores) to H2 type (characteristic of tubular pores which contain narrow constriction or closed pores) is observed with the increase in titania loading (Fig. S1A†). This evolution suggests a loss in pore surface regularity as titania loading increases. Indeed, the formation of nanometric clusters deposited on the surface of the cylindrical pores of the silica host support would lead to the formation of constrictions, with the previously described consequences on the hysteresis shape. It is important to note that the formation of such constrictions will result in some errors on the pore size value as determined on the N_2 desorption branch, due to the artificial delay of desorption generated by the constrictions. Nevertheless, we can consider that the error will be similar for all the samples, allowing the comparison between the different samples even if values of pore sizes given in Table 1 are slightly underestimated.

Deposition of the titania phase in the silica porosity also results in some changes in physical properties (Table 1). The pore volume decreases linearly with the TiO_2 loading (Fig. S3A†). Taking into account the density of the anatase phase equal to 3.72 g cm^{-3}, it is possible to determine a theoretical pore volume decrease (dV_{theo}, Table 1). Thus, 1 g of silica can contain 4.2 g of TiO_2 inside the porosity, corresponding to 81 wt% of TiO_2 loading (assuming the formation of a nonporous titania phase in the silica porosity). The experimental mesopore volume decrease (Table 1) remains always close to the theoretical one, suggesting a satisfying dispersion of the titania inside the silica pore network, with limited pore plugging. Except in the case of the 10Ti-SBA-c400 sample which presents a bimodal mesopore distribution, a monomodal pore size distribution seems to be obtained. As for the pore volume, a linear decrease in pore size with titania loading is obtained (Fig. S3B†) supporting the homogeneous dispersion of titania in the pores.

Surprisingly, all the nanocomposites exhibit almost constant SSA (450–480 m^2 g^{-1}) whatever the titania loading (Table 1 and Fig. S3B†), close to the value measured for the host support (470 m^2 g^{-1}). The possibility of increasing the TiO_2 loading while keeping the SSA constant suggests that the loss of surface area of the silica support due to the titania deposition is nearly compensated by the surface area generated by the titania phase. Finally, micropore volume evolution is presented in Table 1 and in Fig. S3A†. Impregnation of titania at low loading (up to 20 wt%, *V*2 in Table 1) results in a decrease in total micropore volume while further increase in micropore volume, up to a value higher than that of the initial one, is observed with the loading increase (55Ti-SBA-c400). This experimental result suggests that titania impregnation first results in the clogging of the micropore of the silica support, and that some additional micropore volume is generated by the titania phase itself at higher titania loading, possibly generated by arrangement between titania nanoparticles.

In conclusion, the physical properties suggest the formation of small titania nanoparticles dispersed inside the silica porosity, while the limited particle size of the phase formed is suggested to be responsible for the high surface areas maintained and the limited pore plugging.

Table 1. Physical properties of the parent silica support and titania-based nanocomposites.

Sample	% TiO_2	T Calc. / °C	S_{BET}/ $m^2.g^{-1}$	V_1[a] / $cm^3.g^{-1}$	V_2[b] / $cm^3.g^{-1}$	dV_{exp}[c]/ %	dV_{theo}[d]/ %	D_p[e]/ nm	d_{100}/ nm	Wall thickness[f]/ nm	Crystal. phase – d_{XRD}[g]/ nm
SBA	0	550	470	1.13	0.061	0	0	9.7	9.1	0.8	-
10Ti-SBA	10	400	480	1.03	0.037	8.85	12.3	8.5 – 9.4	9.2	2.1 – 1.2	n.d.
20Ti-SBA	20	400	446	0.88	0.025	22.1	24.7	9.1	9.5	1.7	n.d.
		600	370	0.78	0.034	-	-	9.4	9.3	1.3	n.d.
		800	350	0.75	0.020	-	-	8.8	9.5	2.2	anatase
38Ti-SBA	38	400	464	0.57	0.066	49.5	46.9	7.0	9.6	4.1	n.d.
55Ti-SBA	55	400	482	0.47	0.072	58.4	67.9	6.3	9.6	4.8	n.d.
		600	228	0.36	0.008	-	-	7.0	9.0	3.4	anatase – 8.1
		800	204	0.35	0.001	-	-	7.0	9.1	3.5	anatase – 10.3

[a], V_1 is the mesopore volume measured at $P/P_0 = 0.97$; [b], V_2 is the micropore volume extrapolated from the t-plots; [c], dV_{exp} is the fraction of pore volume decrease calculated from the experimental datas; [d], dV_{theo} is the theoretical pore volume decrease assuming the formation of a non porous TiO_2 film on the silica pore surface; [e], D_p obtained using the NLDFT theory on the desorption branch; [f], wall thickness calculated by a_0-Dp where a_0 is calculated for a hexagonal system following the equation $a_0 = (2*d_{100})/\sqrt{3}$; [g], crystal phase identified by XRD (n.d.: no phase detected), and d_{XRD} the crystal domain size evaluated from the X-ray line broadening using the Scherrer equation.

Nanocomposite structure

Small-angle X-ray diffraction patterns evidence the maintain of the hexagonal pore structure after the impregnation-calcination step of the composites (Fig. S2A†). Indeed, the (100) reflection of the hexagonal structure at $2\theta = 0.98 \pm 0.05°$ is still visible for the four nanocomposites. The two low intensity reflections corresponding to the (110) and (200) planes are still visible for 10- and 20Ti-SBA-c400, but their relative intensities decrease with increasing titania loading and are not visible at high titania loadings. Also, the disappearance of these two reflections can be attributed to the interference by increasing diffractions from titania which do not consist in ordered mesostructure. The lattice spacing, calculated from the (100) reflection, is found to slightly increase with the titania loading from 9.1 nm for the SBA support to 9.6 nm for the 55Ti-SBA-c400 sample. A progressive increase in wall thickness is then observed with titania loading (Table 1).

No external aggregates or external surface titania enrichment are observed by TEM (Fig. 1C–D). EDX spectroscopy analysis performed on several silica grains suggests a satisfying repartition of the titania phase inside the silica pores with almost constant TiO_2/SiO_2 mass ratio, close to the bulk ones. Focusing on the pores allows detection of the crystallized particles of size ranging from 2 to 5 nm (examples given for 20Ti-SBA-c400 and 55Ti-SBA-c400, Fig. 1E–F) suggesting that the titania phase is deposited in the form of fine particles in the pores, as suggested by the N_2-sorption analyses. Consequently, TiO_2 particles depositing on the surface of the silica pore can explain the increase in wall thickness observed with the titania loading increase. While TEM analysis suggests the presence of crystallized nanoparticles, no diffraction peaks of TiO2 (anatase, brookite or rutile) can be detected in the 10–80° region, whatever the sample analyzed (Fig. S2B†). Only some poorly defined peaks are hardly detected in the baseline fluctuation for the 55Ti-SBAc400 sample.

Raman analyses were conducted to conclude on the titania structure in the 10-, 20-, 38- and 55Ti-SBA-c400 composites (Fig. 2A). The Raman spectrum of a reference TiO_2 sample (P25 Degussa), calcined at 400 °C, is added for sake of comparison (Fig. 2). The P25 spectrum shows the presence of five characteristic Raman lines, observed at 143 cm^{-1} (E_g), 197 cm^{-1} (E_g), 397 cm^{-1} (B_{1g}), 517 cm^{-1} (B_{2g}),

and 639 cm^{-1} (E_g) which can be assigned to the E_g, E_g, B_{1g}, A_{1g}+B_{1g} and E_g Raman-active fundamentals of TiO_2 anatase.[52,53] The E_g modes observed at 143, 197, and 639 cm^{-1} in the P25 sample spectrum will be noted $E_g(1)$, $E_g(2)$ and $E_g(3)$ modes, respectively. The band observed at 517 cm^{-1} results from an overlapping of two bands of A_{1g} and B_{1g} symmetry, which could be resolved only at low temperature.[52] A broad hump observed at 447 cm^{-1} and a shoulder around 615 cm^{-1} (marked and noted R, Fig. 2A) are characteristic of the E_g and A_{1g} modes of the rutile phase, respectively which shows that rutile is mixed to anatase in the P25 sample.[53]

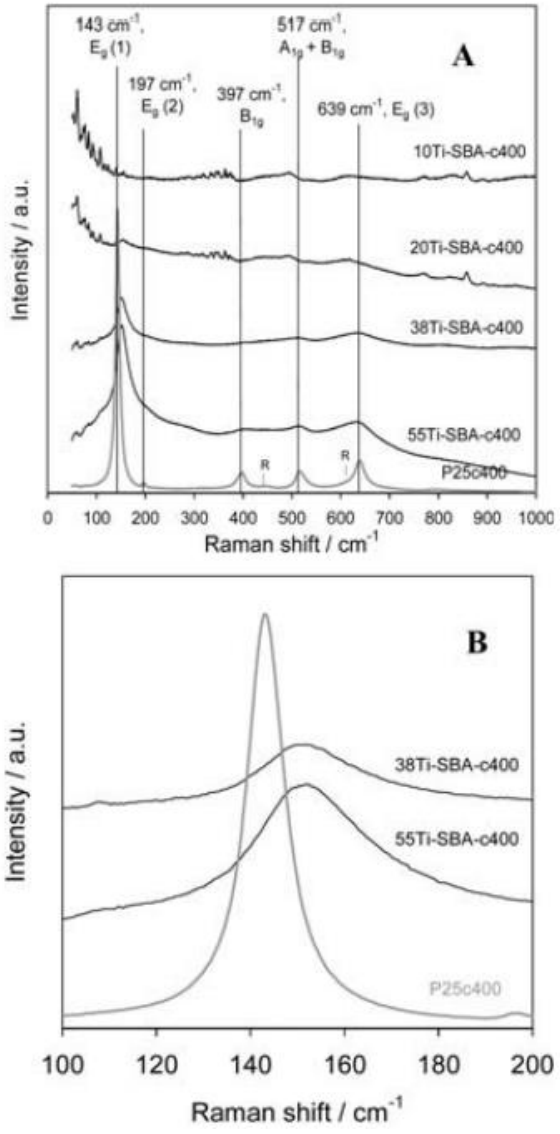

Fig. 2. (A) Evolution of the Raman spectra with the titania loading in the nanocomposites after calcination at 400°C. R: rutile contributions. (B) $E_g(1)$ mode of anatase.

No signal can be detected for the 10Ti-SBA-c400 sample. Both the titania content and Raman cross section of modes to be observed are too weak, combined with the difficulty to observe Raman features

due to the intense light scattering by the small particle size distribution of the white material. For the other three samples, Raman features characteristic of the anatase phase can be observed. However, important broadening, peak shifts and intensity variations of the bands are noticed (Fig. 2A). These effects are much more pronounced for the $E_g(1)$ mode: Fig. 2B shows a comparison of the $E_g(1)$ peaks of 38-, 55Ti-SBA-c400 and P25c400. The $E_g(1)$ peaks of 38-, 55Ti-SBA-c400 shift to blue, broaden asymmetrically (high Raman shift) and encounter a decrease in intensity. Furthermore, Raman shifts and peak width data are linearly correlated (not shown), as observed for other anatase nanocrystallites.[54] This matches the main experimental observations associated with drastic changes in particle size down to 10 nm and less made in the study of anatase nanoparticles.[54-58] In our case, where titania is not the sole phase under consideration, the intensity variation of the peaks is due to several contributions: one originates from the dilution of anatase in SBA-15; the other one, may be in a lesser extent, comes from the nanometer size of the anatase crystallites. In addition to the broadening pointed above, a small redshift (blueshift) is seen for $E_g(2)$ (B_{1g}) modes when applicable within the spectral resolution. Both A_{1g} + B_{1g} and $E_g(3)$ modes show a redshift. These lineshape changes of the Raman peaks were interpreted by different mechanisms such as non-stoichiometry by oxygen deficiencies or the disorder induced by minor phases, pressure and phonon confinement effects, the latter being described as the most important effect.[57]

It uses the q vector relaxation model (QVRM) which is described in details elsewhere.[55] Summarizing, it is considered in this model that nanocrystalline solid state with finite sized crystals presents an intermediate behavior between “infinite” crystalline state with long-range order and amorphous state. Although using $E_g(1)$ Raman shifts gave quite good results, a much better agreement is obtained by Swamy et al.[54] using this model between their experiments, as well as experimental results of other different groups, and QVRM for FWHM of $E_g(1)$ peak versus crystallite size drawn by Kelly et al.[55] This result motivates the choice to use this curve herein as a calibration curve to estimate the anatase crystallite size of our samples from the FWHM of $E_g(1)$ peaks obtained, with a particular interest in the samples for which it was not possible to measure crystallite size using X-ray diffraction.

The peak widths, peak position and the subsequent crystallite size thus estimated are gathered in Table 2. The crystal sizes calculated using the QVRM curve[58] are evaluated at 4.4 nm and 4.0 nm for the 38Ti-SBA-c400 and 55Ti-SBA-c400 samples, respectively.

Table 2. Peak widths and peak position of Raman $E_g(1)$ modes obtained for the different composites. Crystallite size of the anatase phase occluded in the SBA15 as deduced from $E_g(1)$ mode FWHM of anatase Raman feature using QVRM curve drawn by Kelly et al.[55]

Sample	% TiO_2	T Calc. / °C	$E_g(1)$ TiO_2 anatase peak		Crystallite size – $d_{E_g(1)}$ / nm
			Raman shift / cm^{-1}	FWHM / cm^{-1}	
20Ti-SBA	20	400	154.6	n. d.	n. d.
		600	154.1	30.0	4.0
		800	153.5	29.0	4.1
38Ti-SBA	38	400	151.4	27.0	4.4
55Ti-SBA	55	400	151.9	30.0	4.0
		600	145.8	16.0	7.4
		800	144.7	13.6	9.0

n.d.: no significant peak detected

Unfortunately, the poor definition of the Raman spectrum for the two low loading composites avoids the evaluation of the crystallite size in these two samples. It can however be noted that the crystal sizes calculated for the 38- and 55-Ti-SBA-c400 samples are in agreement with the observations made by TEM (Fig. 1), and confirm the formation of anatase nanoparticles in the composites at sizes below the detection limit of the XRD.

Nanocomposite surface properties

Following usual convention,[67,68] stretching ν(OH) frequencies (higher than 3600 cm^{-1}) of isolated OH groups are designated as type I (terminal), type II (bridging =OH), and type III (multi-centered, ≡OH). Spectra of the nanocomposites in the OH stretching region (3900-3300 cm^{-1}), normalized to unit weight to allow comparison, are reported in Fig. 3A. The spectrum of SBA15 exhibits a sharp band at 3745 cm^{-1}, assigned to isolated SiOH species as previously reported.[69-71] A tail on the low frequency side, that can be attributed to surface site heterogeneity (*i.e.* isolated, geminal and vicinal SiOH species) as can be

expected for silica outgassed at low temperature (400 °C in this work), is observed. The impregnation-calcination cycle of TiO_2 results in a decrease of the component at 3745 cm^{-1} intensity (SiOH) and in a shift toward the low wavenumbers of the OH stretching vibration. Indeed, the ν(OH) mode shifts from isolated silanol at 3745 cm^{-1} (SBA) to 3741 cm^{-1} (55Ti-SBA-c400), band attributed to isolated/geminal silanol couples.[59] A component at 3720 cm^{-1} is also observed over the nanocomposites. As already reported in the literature,[64,65] this band can be assigned to TiOH species. Indeed, Zaki et al.[65] suggest that this band can be ascribed to terminal Ti–OH group bound to Ti^{4+} site exposed on the surface of anatase crystal domains. A second broad band, located at 3670 cm^{-1}, is also observed. Its intensity is also found to increase with the titania loading. This band can be ascribed to acidic OH groups,[66] even if other authors prefer to assign this band to Ti-OH-Ti groups.[67] As previously mentioned, the intensity of the isolated silanols band at 3745 cm^{-1} is strongly affected by titanium loading. Evolution of the intensity band with the titania loading suggests that OH groups induced by the titania grafting easily grow on the silica surface and lead to the formation of Ti-OH-Ti species (bands at 3720 and 3670 cm^{-1}). Note that the increase in this last new species leads to a preferential decrease in isolated SiOH species, more than to a 'bound' geminal silanol consumption.

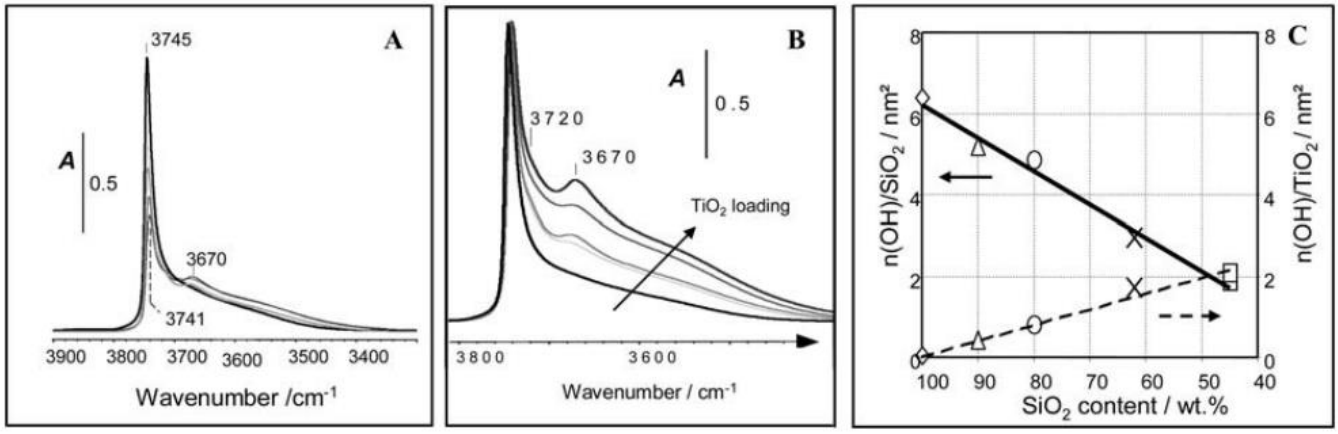

Fig. 3. Evolution of the FT-IR spectra of the nanocomposites with the titania loading. (A), IR spectra in the ν(OH) region of modified silica activated at 400 C; (B) spectra normalized at similar SiOH band intensity; (C), Relationship between the SiOH and the residual TiOH versus the amount of SiO_2 in the composites.

OH surface density was determined using the Beer-Lambert law on the hydroxyl region area, assuming constant ε (1 $cm.mol^{-1}$) for all SiOH types.[59] OH surface densities are summarized in Table 3,

and plotted as a function of titania loading in the composites in Fig. 3C. Pure silica sample presents a OH surface density of 6.3 $OH.nm^{-2}$ (Table 3), a value close to those reported in the literature. Indeed, 4.6 $OH.nm^{-2}$ is reported by Armistead et al.[68] and Peri et al.,[69] while Fripiat et al.[70] estimated OH densities over silica samples ranging from 6.70 $OH.nm^{-2}$ to 7.85 $OH.nm^{-2}$. The density of SiOH is found to decrease linearly from 6.3 $OH.nm^{-2}$ (SBA) to 1.8 $OH.nm^{-2}$ (55Ti-SBA) with the increase in titania loading. As the global area of OH region remain constants for all solids (ν(OH) region from 3900 to 3300 cm^{-1}, Fig. 3A), the TiOH surface density of composites can be calculated from the TiOH area obtained by substraction of the residual SiOH to the total OH group area. Note that ε, the molar absorption coefficient, is not constant depending on the nature of the hydroxyl (*i.e.* SiOH or TiOH). Surface OH densities between 5.4 and 11.3 $OH.nm^{-2}$ are reported for the P25 Degussa titanium oxide.[71,72] Consequently the molar absorption coefficient of TiOH species can be estimated from the P25 infrared spectra (not shown), and is assumed to be close to 2 $cm.mol^{-1}$. Calculated surface TiOH density is found to linearly increase with the titania loading, from 0 $OH.nm^{-2}$ (SBA) to 2.0 $OH.nm^{-2}$ (55Ti-SBA) (Fig. 3C). This result shows, as suggested by the weak variation of the specific surface area whatever the titania loading (Table 1), that titania cluster size remains almost constant in all the nanocomposites. In addition, Fig. 3C shows that the formation of one TiOH in the composite is accompanied by a loss of two SiOH. This result is in accordance with the IR spectra reported in Fig. 3A that shows the emergence of a broad band at 3670 cm^{-1} assigned to bridging Ti–OH–Ti species, with the decrease of the isolated SiOH band intensity.

Table 3. SiOH and TiOH surface concentration obtained for the different nanocomposites.

Sample	% TiO_2	T Calc. / °C	SiOH		TiOH	
			Area / cm^{-1}	n (OH) / nm^2	Area / cm^{-1}	n (OH) / nm^2
SBA	0	550	34.5	6.3	0	0
10Ti-SBA	10	400	28.6	5.1	4.2	0.4
20Ti-SBA	20	400	24.9	4.8	7.9	0.8
38Ti-SBA	38	400	15.4	2.9	18.4	1.7
55Ti-SBA	55	400	10.2	1.8	22.7	2.0

In conclusion, the TiOH species present on the surface of nanocomposites are essentially similar to those present on the surface of conventional titania. Furthermore, FTIR analysis supports the interpretation of titania cluster having anatase structure with similar crystal size whatever the composite, that is consistent with the information deduced from Raman spectroscopy and from N_2 sorption experiments.

Thermal stability of the nanocomposites

Results of characterization suggest that the nanocomposites calcined at 400°C maintain an open mesopore structure, originating from the silica support, and consist of anatase nanocrystals (<5 nm, as determined by Raman spectroscopy) supported on the pore surface. Thermal stability of the nanocomposite is studied over two selected samples (20Ti-SBA and 55Ti-SBA) for temperatures between 400°C and 800°C. First, the N_2 adsorption-desorption isotherm shape remains almost unchanged (type IV according to the IUPAC classification) whatever the sample and the calcination temperature (example of 55Ti-SBA, Fig. 4). Nevertheless, physical properties of the two composites evolve differently, while physical properties of the silica support are only slightly altered by the increase in calcination temperature (Table 1).

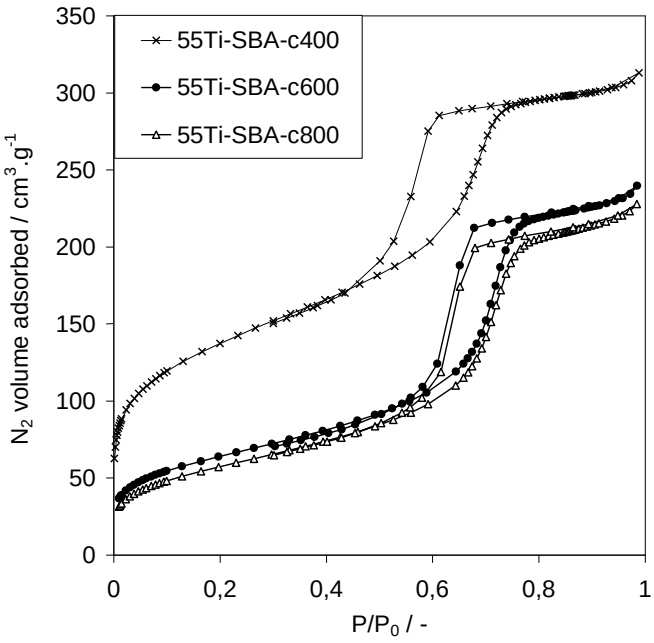

Fig. 4. Effect of the calcination temperature on the N_2 adsorption-desorption isotherm. Example of 55Ti-SBA.

Case of 20Ti-SBA

The increase in calcination temperature from 400°C to 800°C results in a decrease of 20% and 15% of the surface area and mesopore volume, respectively. Then, a surface area of 350 m^2 g^{-1} is maintained after stabilization at 800°C. The preservation of attractive physical properties offered by the nanocomposites after calcination at 800°C can obviously be related to their typical morphology, and the contribution of the silica surface to the total surface area measured. The hexagonal pore structure of the silica host support is still maintained, as observed by small angle XRD (not shown). Focus on the channels allows to still detect small titania crystallized nanoparticles (<5nm) event at 800°C (Fig. S4A†).

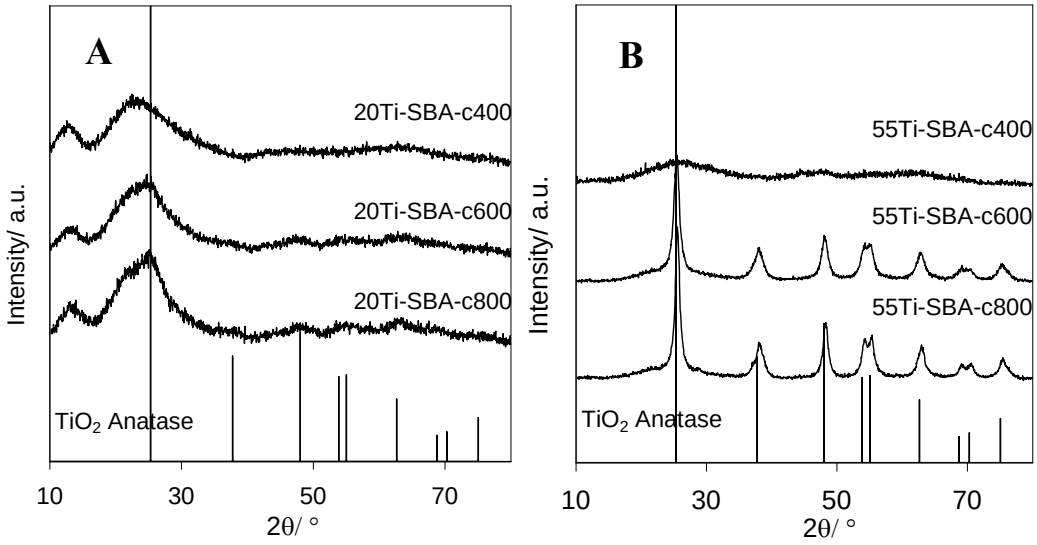

Fig. 5 Evolution of the X-ray diffraction patterns with the calcination temperature of the composite. (A) 20Ti-SBA; (B) 55Ti-SBA.

The limited sintering of the titania nanocrystals with the calcination temperature increase is confirmed by XRD (Fig. 5A) and Raman spectroscopy (Table 2 and Fig. S5A†). Indeed, only broad and poorly defined reflections of the anatase structure are detected by XRD on the 20Ti-SBA sample calcined at 800°C. In addition, anatase $E_g(1)$ Raman peaks modes of the nanocomposite are slightly red shifted from 800°C to 400°C, while the corresponding FWHM is weakly decreasing from 800°C to 600°C (Table 2). The linear correlation between Raman shift and FWHM allows the assumption that the FWHM at 400°C should be hardly superior to the one at 600°C, hence a weakly smaller crystallite size could be expected at 400 C. Therefore, crystallite size remains at ~4 nm, when evaluated using the QVRM curve (Table 2).

In conclusion, the increase in calcination temperature up to 800°C of the 20Ti-SBA sample does not result in important physical and morphological modifications, and only a limited anatase nanodomain sintering is observed. The morphology of this nanocomposite is depicted in Fig. 6, with titania nanodomains dispersed inside the silica pore structure, with minor effect of the calcination temperature, suggesting sufficient interaction between anatase nanoparticles and silica surface to limit crystal growth upon increasing the thermal treatment.

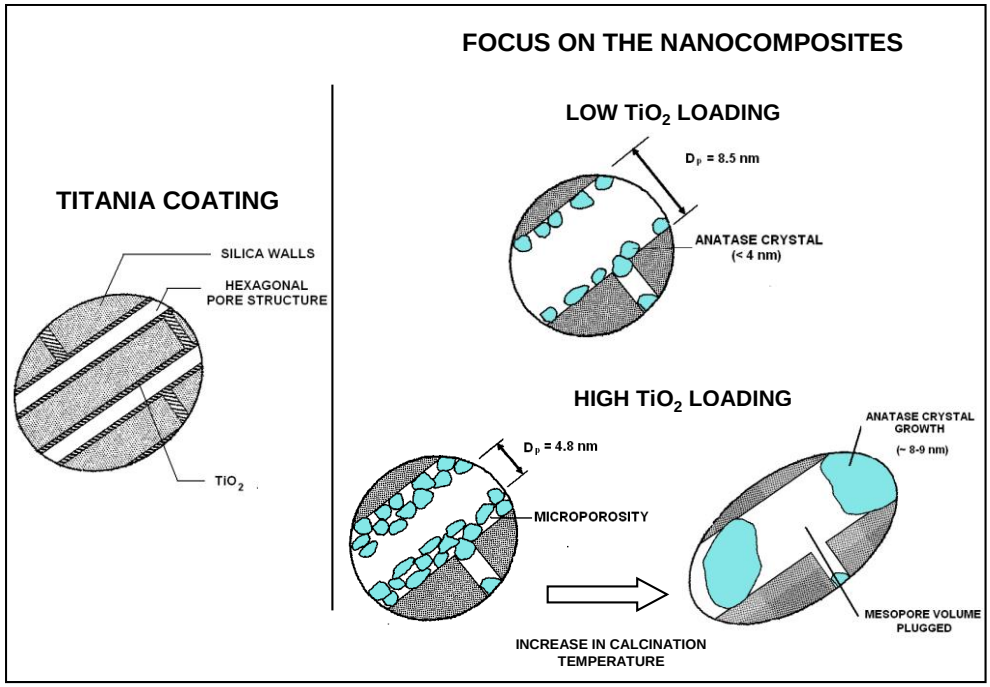

Fig. 6. Scheme of the nanocomposite morphology evolution with the TiO_2 loading and calcination temperature.

Case of 55Ti-SBA

Results obtained over the 55Ti-SBA nanocomposite strongly differ from those obtained for the last sample. While the N_2 adsorption–desorption isotherm shape remains almost unchanged (Fig. 4), important decreases in surface area (58%) and pore volume (25%) are obtained while increasing the calcination temperature from 400°C to 800°C (Table 1). These changes in the physical properties are mainly related to modifications of the titania phase, since the properties of silica are only slightly altered by the calcination temperature increase (Table 1). Small angle X-ray diffraction suggests that these modifications do not originate from the loss of silica pore structure periodicity, since the (100) reflection of the hexagonal structure is still visible whatever the calcination temperature (not shown). TEM analysis allows the detection of anatase nanoparticles. These particles seem to be always located inside

the silica pores (Fig. S4B†), even if a diffusion of a part of titania outside the pores upon increasing the thermal treatment cannot be excluded. The increase in calcination temperature also results in important modification of both X-ray diffraction patterns (Fig. 5B) and Raman spectra (Fig. S5B†). Indeed, well-defined reflections of anatase phase are observed in Fig. 5B after calcination at 600°C. Evaluation of the mean particle size from X-ray line broadening leads to sizes of 8.1 nm and 10.3 nm, after calcination at 600°C and 800°C respectively. These sizes are close to the NLDFT pore size measured for the silica support alone (9.7 nm, Table 1). Such particles located in the pore obviously lead to important pore clogging, and can account for the important decreases in pore volume and SSA measured over this sample. Raman spectroscopy confirms the presence of a well-crystallized anatase phase after calcination at 400°C, 600°C and 800°C (Fig. S5B†). The decrease in FWHM combined with a red shift of the Raman peaks with increasing calcination temperature is observed, confirming the progressive crystallite size increase. The values of crystal size, evaluated from Raman spectroscopy, are 7.4 nm and 9.0 nm after calcination at 600°C and 800°C respectively. These values are in agreement with those obtained using the Scherrer equation (Table 1).

Thus, the composite calcined at low temperature (400°C) presents titania nanodomains dispersed inside the silica porosity. The increase in calcination temperature up to 600°C leads to the sintering of these nanodomains to ~8–10 nm domains in the silica pore, resulting in important pore plugging (and consequently into important decreases in SSA and pore volume), as shown in Fig. 6. From the obtained results, it seems that the crystal growth is physically limited by the silica inorganic walls (similar crystal size and support pore size). Contrary to conventional P25 titania (Raman analyses after calcination at 600°C and 800°C, not shown), and contrary to TiO_2 nanocrystals annealed up to 690°C with an almost total transformation into rutile at 690°C,[65] crystallization of the rutile phase is not observed for 55Ti-SBA. Indeed, no E_g or A_{1g} most pronounced modes of rutile observed at ca. 444 and 611 cm^{-1} respectively, can be seen on any spectrum (Fig. S5B†). Both the nature of the silica support,[81] and the reduced size of its porosity (<10 nm) that leads to a maximum titania crystal size by confining effect, can account for the lack of anatase to rutile transition even at 800°C. Indeed, rutile macrocrystals are

reported to be thermodynamically more stable than the two other polymorphs while the nanocrystalline (<14 nm) anatase and brookite polymorphs are more stable than rutile.[82,83]

Oxygen mobility in the nanocomposites

The $^{18}O/^{16}O$ exchange reaction is used to evaluate the titania nanoclusters reactivity. It is first verified that silica alone does not present any noticeable activity up to 800°C.

The evolution of the fraction in ^{18}O in the gas phase (a) with the reaction temperature is presented in Fig. 7. The values of a, number of atom exchanged (N_{ex}) and fraction of oxygen from the solid exchanged (O_{ex}) at the end of the experiment are summarized in Table 4.

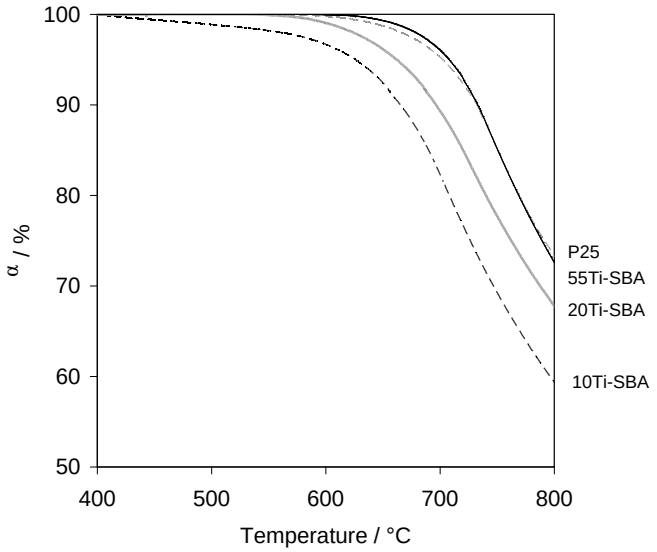

Figure 12. Evolution of the fraction of ^{18}O in the gas phase with the reaction temperature obtained for the nanocomposites and the reference P25 sample.

The P25 reference sample presents low activity. Indeed, the exchange started at ~580 C (Fig. 7). At the end of the exchange reaction (800°C), the fraction of ^{18}O remaining in the gas phase is measured at 73.3% (Table 4), given a fraction of oxygen exchanged from the solid of only 57%. The 55Ti-SBA sample presents a similar behaviour in exchange than the P25 sample, with almost similar values of a and O_{ex} at the end of the exchange reaction (Fig. 7, Table 4). Thus, similar oxygen reactivities are obtained between the two samples even if the two solids present different crystallographic and morphologic features. Indeed, small anatase nanodomains (9 nm, Table 2) are obtained on the 55Ti-SBA-c800 sample, while P25 presents large rutile crystals at the same temperature. Nevertheless, the

low activity obtained on the 55Ti-SBA sample can be related to the pore plugging phenomenon occurring on this sample when calcination temperature exceeds 600°C.

Table 4. Measure of the oxygen reactivity in the different composites using the oxygen isotopic exchange reaction.

Sample	α^a / %	N_{ex}^b / 10^{20} at.g^{-1}	O_{ex}^c / %
10Ti-SBA	59.3	76.9	97
20Ti-SBA	67.8	62.5	78
55Ti-SBA	72.6	49.9	57
P25	73.3	48.9	57

[a], α is the fraction of ^{18}O in the gas phase at 800 °C; [b], N_{ex} is the number of oxygen atoms exchanged at 800 °C; [c], O_{ex} is the fraction of oxygen from the solid exchanged at 800 °C.

Thus, the limited access of the titania crystals, isolated in the silica porosity can be a reason of the low exchange activity measured for this sample. Significantly higher exchange activities are measured for the 10Ti-SBA and 20Ti-SBA samples, with values of ^{18}O in the gas phase at the end of the exchange reaction of 59.3% and 67.8% respectively (Table 4). This increase in reactivity is also clearly observed by the shift to the lower temperature of the beginning of the exchange reaction (Fig. 7), a phenomenon clearly observed for the 10Ti-SBA for which the exchange reaction starts since 400°C. At the end of the exchange reaction, considerably higher fractions of oxygen exchanged (O_{ex}) are obtained over these two solids than over the P25 and 55Ti-SBA samples. Indeed, a O_{ex} value of 78% is obtained for the 20Ti-SBA sample, while 97% of the oxygen from the 10Ti-SBA sample is available for exchange (Table 4). It is however difficult to explain the difference in activity between the 10Ti-SBA and 20Ti-SBA samples since the form of the titania phase in the 10Ti-SBA cannot be deduced either from XRD or from Raman spectroscopy. We suppose that the higher activities obtained for these two samples, with respect to that of the 55Ti-SBA sample, is related to the limited sintering occurring on these two solids, allowing the maintain of a high titania accessibility. This titania accessibility is a key parameter since the exchange reaction mechanism supposes adsorption and dissociation of the $^{18}O_2$ molecules on the oxide support.[84] In conclusion, high oxygen mobilities are obtained for the two samples presenting limited sintering, showing the high reactivity of titania nanodomains.

Conclusion

This work presents the results of the synthesis, characterization and reactivity of titania nanodomains. Titania nanodomains (<5 nm) dispersed in the silica hexagonal pore structure, with no visible segregation outside the silica, are obtained. Using the proposed procedure, nanocomposites having up to 55 wt% of TiO_2 loading are prepared. Even at high titania loading, the titania nanodomain size remains limited, and no important pore plugging can be evidenced when calcined at low/intermediate temperature (400°C in this work). Due to the limited TiO_2 cluster size, high surface area (~450 m^2 g^{-1}) can be maintained whatever the titania loading. Characterizations support the formation of crystallized anatase particles, and FT-IR evidences surface properties similar to that of conventional bulk titania reference. Thermal stability evolves differently, depending on the titania loading. Indeed, surface area and pore volume of the high titania loading nanocomposite are found to strongly decrease while increasing calcination temperature from 400°C up to 800°C. Characterization of the solid allows to explain these modifications by the sintering of the <5 nm anatase nanodomains into ~8–10 nm anatase domains when calcination temperature exceeds 600°C. Such crystal size, close to the pore size of the host support, results in important pore plugging. High thermal stability is however obtained over the low titania loading nanocomposite, with a limited crystal growth while increasing the calcination temperature up to 800°C. A composite having high surface area and high pore volume is obtained, making the physical properties of this sample attractive with regard to a potential use as catalyst or catalyst support. Significantly higher oxygen reactivities are obtained for the samples which do not suffer from titania sintering (titania loading <20 wt%) , and the fraction of oxygen available for the exchange reaction is found to reach 97% at 800 C on the 10Ti-SBA sample, while only 57% of the oxygen exchanges on the P25 reference and 55Ti-SBA samples at the same temperature. A high oxygen reactivity is clearly shown for stable titania nanoparticles (<5 nm).

ACKNOWLEDGMENT

The Région Poitou-Charentes, France, is gratefully acknowledged for financial support of this work through a Ph.D. grant (M. Bonne).

NOTES and REFERENCES

(1) Chen, X.; Mao, S. S. *Chem. Rev*., **2007**, *107*, 2891.

(2) Reyes-Coronado, D.; Rodriguez-Gattorno, G.; Espinosa-Pesqueira, M.; Gardner, J. M.; Meyer, G. J.; Oskam, G. *Proceeding of SPIE*, **2007**, 6650.

(3) Koelsch, M.; Cassaignon, S.; Guillemoles, J. F.; Jolivet, J. P. *Thin Solid Films*, **2002**, *403-404*, 312.

(4) Zhang, H.; Banfield, J. F. *J. Mater. Chem.*, **1998**, *8*, 2073.

(5) Ye, X.; Chen. D.; Li, K.; Shah, V.; Kesmez, M.; Vajifdar, K. *Chem. Eng. Commun*., **2007**, *194*, 368.

(6) Vlachos, P.; Stathatos, E.; Lyberatos, G.; Lianos, P. *Catal. Commun.*, **2008**, *9*, 1987.

(7) Grosso, D.; Soler-Illia, G. J. de A. A.; Crepaldi, E. L.; Cagnol, F.; Sinturel, C.; Bourgeois, A.; Brunet-Bruneau, A.; Amenitsch, H.; Albouy, P. A.; Sanchez, C. *Chem. Mater.*, **2003**, *15*, 4562.

(8) Hagfeldt, A.; Grätzel, M. *Chem. Rev.*, **1995**, *95*, 49.

(9) Inoue, S.; Muto, A.; Kudou, H.; Ono, T. *Appl. Catal. A*, **2004**, *269*, 7.

(10) Barrera, M. C.; Escobar, J.; Reyes, J. A.; Cortés, M. A.; Viniegra, M.; Hernandez, A. *Catal. Today*, **2006**, *116*, 498.

(11) Luo, S.; Falconer, J. L. *J. Catal*., **1999**, *185*, 393.

(12) Cao, L.; Gao, Z.; Suib, S. L.; Obee, T. N.; Hay, S. O.; Freihaut, J. D. *J. Catal.*, **2000**, *196*, 253.

(13) Elshafei, G. M. S.; Philip, C. A.; Moussa, N. A. *Micro. Meso. Mater*., **2005**, *79*, 253.

(14) Iwasaki, M.; Hara, M.; Ito, S. *J. Mater. Sci. Lett.*, **1998**, *17*, 1769.

(15) Aguado-Serrano, J.; Rojas-Cervantes, M. L.; *Micro. Meso. Mater*., **2006**, *88*, 205.

(16) Liu, C.; Fu, L.; Economy, J. *J. Mater. Chem*., **2004**, *14*, 1187.

(17) Sclafani, A.; Palmisaro, L.; Schiavello, M. *J. Phys. Chem.*, **1990**, *94*, 829.

(18) Antonelli, D. M. *Micro. Meso. Mater.*, **1999**, *30*, 315.

(19) Yoshitake, H.; Sugihara, T.; Tatsumi, T. *Chem. Mater*., **2002**, *14*, 1023.

(20) Yoshitake, H.; Tatsumi, T. *Chem. Mater.*, **2003**, *15*, 1695.

(21) Cassiers, K.; Linssen, T.; Mathieu, M.; Bai, Y. Q.; Zhu, H. Y.; Cool, P.; Vansant, E. F. *J. Phys. Chem. B*, **2004**, *108*, 3713.

(22) Yang, P.; Zhao, D.; Margolese, D. I.; Chmelka, B. F.; Stucky, G. D. *Chem. Mater*., **1999**, *11*, 2813.

(23) Alberius, P. C. A.; Frindell, K. L.; Hayward, R. C.; Edward, J. K.; Stucky, G. D.; Chmelka, B. F. *Chem. Mater*., **2002**, *14*, 3284.

(24) Luo, H.; Wang, C.; Yan, Y. *Chem. Mater.*, **2003**, *15*, 3841.

(25) Smarsly, B.; Grosso, D.; Brezesinski, T.; Pinna, N.; Boissière, C.; Antonietti, M.; Sanchez, C. *Chem. Mater.*, **2004**, *16*, 2948.

(26) Haseloh, S.; Choi, S. Y.; Mamak, M.; Coombs, N.; Petrov, S.; Chopra, N.; Ozin, G. A. *Chem. Commun*., **2004**, 1460.

(27) Kartini, I.; Meredith, P.; Diniz Da Costa, J. C.; Lu, G. Q. *J. Sol-Gel. Sci. Technol*., **2004**, *31*, 185.

(28) Kartini, I.; Menzies, D.; Blake, D.; Da Costa, J. C. D.; Meredith, P.; Riches, J. D.; Lu, G. Q. *J. Mater. Chem.*, **2004**, *14*, 2917.

(29) Eiden-Assmann, S.; Widoniak, J.; Maret, G. *Chem. Mater.*, **2004**, *16*, 6.

(30) Widoniak, J.; Eiden-Assmann, S.; Maret, G. *Prog. Colloid Polym. Sci.*, **2004**, *129*, 119.

(31) Wu, C.-W.; Ohsuna, T.; Kuwabara, M.; Kuroda, K. *J. Am. Chem. Soc.*, **2006**, *128*, 4544.

(32) Khushalani, D.; Ozin, G. A.; Kuperman, A. *J. Mater. Chem.*, **1999**, *9*, 1491.

(33) Soller-Illia, G. J. de A. A.; Louis, A.; Sanchez, C. *Chem. Mater*., **2002**, *14*, 750.

(34) Shibata, H.; Ogura, T.; Mukai, T.; Ohkubo, T.; Sakai, H.; Abe, M. *J. Am. Chem. Soc*., **2005**, *127*, 16396.

(35) Thieme, M.; Schüth, F. *Micro. Meso. Mater*., **1999**, *27*, 193.

(36) Marchesini, F. A.; Irusta, S.; Querini, C.; Miro, E. *Appl. Catal. A*, **2008**, *348*, 60.

(37) Zeleňák, V.; Hornebecq, V.; Mornet, S.; Schäf, O.; Llewellyn, P. *Chem. Mater*., **2006**, *18*, 3184.

(38) Dong, W.; Sun, Y.; Wee L. C.; Hua, W.; Lu, X.; Shi, Y.; Zhang, S.; Chen, J.; Zhao, D. *J. Am. Chem. Soc.*, **2007**, *129*, 13894.

(39) Bérubé, F.; Kleitz, F.; Kaliaguine, S. *J. Phys. Chem. C*, **2008**, *112*, 14403.

(40) Bérubé, F.; Kleitz, F.; Kaliaguine, S. *J. Mater. Sci.*, **2009**, *44*, 6727.

(41) Fattakhova-Rohlfing, D.; Szeifert, J. M.; Yu, Q.; Kalousek, V.; Rathousky, J.; Bein, T. *Chem. Mater.*, **2009**, *21*, 2410.

(42) Wang, W.; Song, M. *Mat. Res. Bull.*, **2006**, *41*, 436.

(43) Cozzolino, M.; Di Serio, M.; Tesser, R.; Santacesaria, E. *Appl. Cat. A*, **2007**, *325*, 256.

(44) Lin, Y.-C.; Chang, C.-H.; Chen, C.-C.; Jehng, J.-M.; Shyu, S.-G. *Catal. Commun.*, **2008**, *9*, 675.

(45) Landau, M. V.; Vradman, L.; Wang, X.; Titelman, L. *Micro. Meso. Mater.*, **2005**, *78*, 117.

(46) Roggenbuck, J.; Koch, G.; Tiemann, M. *Chem. Mater.*, **2006**, *18*, 4151.

(47) Royer, S.; Duprez, D.; Kaliaguine, S. *J. Catal.*, **2005**, *234*, 364.

(48) Bonne, M.; Bion, N.; Pailloux, F.; Valange, S.; Royer, S.; Tatibouët, J.-M.; Duprez, D. *Chem. Commun*., **2008**, 4504.

(49) Sing, K. S. W.; Everett, D. H.; Haul, R. H. W.; Moscou, L.; Pierotti, R. A.; Rouquerol, J.; Siemieniewska, T. *Appl. Chem.*, **1985**, *57*, 603.

(50) Kruk, M.; Jaroniec, M.; Ko, C. H.; Ryoo, R. *Chem. Mater.*, **2000**, *12*, 1961.

(51) Ryoo, R.; Ko, C. H.; Kurk, M.; Antochshuk, V.; Jaroniec, M. *J. Phys. Chem. B*, **2000**, *104*, 11465.

(52) Ohsaka, T.; Izumi, F.; Fujiki, Y. *J. Raman Spectrosc.* **1978**, *7*, 321.

(53) Balachandran, U.; Eror, N. G. *J. Solid State Chem.* **1982**, *42*, 276.

(54) Swamy, V.; Kuznetsov, A.; Dubrovinsky, L. S.; Caruso, R. A.; Shchukin, D. G.; Muddle, B. C. *Phys. Rev. B* **2005**, *71*, 184302.

(55) Kelly, S.; Pollak, F. H.; Tomkiewicz, M. *J. Phys. Chem. B* **1997**, *101*, 2730.

(56) Bersani, D.; Lottici, P. P.; Ding, X.-Z. *Appl. Phys. Lett.* **1998**, *72*, 73-75.

(57) Zhang, W. F.; He, Y. L.; Zhang, M. S.; Yin, Z.; Chen, Q. *J. Phys. D: Appl. Phys.*, **2000**, *33*, 912.

(58) Ivanda, M.; Musić, S.; Gotić, M.; Turković, A.; Tonejc, A. M.; Gamulin, O. *J. Mol. Struct.*, **1999**, *480*, 641.

(59) Legrand, A. P.; Hommel, H; Tuel, A.; Vidal, A.; Balard, H.; Papirer, E.; Levitz, P.; Czernichowski, M.; Erre, R.; Van Damme, H.; Gallas, J. P.; Hemidy, J. F.; Lavalley, J. C.; Barrese, O.; Burneau, A.; Grillet, Y. *Adv. Coll. Interf. Sci.*, **1990**, *33*, 91.

(60) Tsyganenko, A. A.; Filimonov, V. N. *J. Mol. Structure*, **1973**, *19*, 579.

(61) Manoilova, O. V.; Dakka, J.; Sheldon, R. A.; Tsyganenko, A. A. *Stud. Surf. Sci. Catal.*, **1995**, *94*, 163.

(62) Knözinger, H.; Huber, S. *J. Chem. Soc. Faraday Trans.* **1998**, *94*, 2047.

(63) Trukhan, N. N.; Panchenko, A. A.; Roduner, E. *Langmuir*, **2005**, *21*, 10545.

(64) Bonelli, B.; Cozzolino, M.; Tesser, R.; Di Serio, M.; Piumetti, M.; Garrone, E.; Santacesaria, E. *J. Catal.*, **2007**, *246*, 293.

(65) Zaki, M. I.; Hasan, M. A.; Al-Sagheer, F. A.; Pasupulety, L. *Coll. Surf. A: Physicochem. Eng. Aspects*, **2001**, *190*, 261.

(66) Widenmeyer, M.; Grasser, S.; Köhler, K.; Anwander, R. *Micro. Meso. Mater.*, **2001**, *44-45*, 327.

(67) Travert, A.; Manoilova, O. V.; Tsyganenko, A. A.; Mauge, F.; Lavalley, J. C. *J. Phys. Chem. B*, **2002**, *106*, 1350.

(68) Armistead, C. G.; Tyler, A. J.; Hambleton, F. H.; Mitchell, S. A.; Hockey, J. A. *J. Phys. Chem.*, **1969**, *73*, 3947.

(69) Peri, J. B.; Hensley, A. L. Jr. *J. Phys. Chem.*, **1968**, *72*, 2926.

(70) Fripiat, J. J.; Uytterhoeven, J. *J. Phys. Chem.*, **1962**, *66*, 800.

(71) Mueller, R.; Kammler, H. K.; Wegner, K.; Pratsinis, S. E. *Langmuir*, **2003**, *19*, 160.

(72) Wang, Z. W.; Wang, T.-J.; Wang, Z. W.; Jin, Y. *J. Coll. Interf. Sci.*, **2006**, *304*, 152.

(73) Haoudi, A.; Dhamelincourt, P.; Mazzah, A.; Drache, M.; Conflant, P.; Lazraq, M. *J. Mater. Chem.* **2000**, *10*, 1001-1005.

(74) Zhang, H.; Banfield, J. F. *J. Mater. Chem.*, **1998**, *8*, 2073.

(75) Zhang, H.; Banfield, J. F. *J. Phys. Chem. B*, **2000**, *104*, 3481.

(76) Hargreaves, J. S. J.; Jackson, S. D.; Webb G. *Isotopes in Heterogenous Catalysis*; Catalytic Science Series – Vol. 4: Imperial College Press, London, UK, 2006.